Extending the depth of field with chromatic aberration for dual-wavelength iris imaging

NIAMH M. FITZGERALD,[1,*] **CHRISTOPHER DAINTY,**[2] **AND ALEXANDER V. GONCHAROV**[1]

[1]*Applied Optics Group, School of Physics, National University of Ireland, Galway, Ireland*
[2]*FotoNation Ltd., Parkmore East Ind. Estate, Ballybrit, Galway, Ireland*
[*]*n.fitzgerald1@nuigalway.ie*

Abstract: We propose a method of extending the depth of field to twice that achievable by conventional lenses for the purpose of a low cost iris recognition front-facing camera in mobile phones. By introducing intrinsic primary chromatic aberration in the lens, the depth of field is doubled by means of dual wavelength illumination. The lens parameters (radius of curvature, optical power) can be found analytically by using paraxial raytracing. The effective range of distances covered increases with dispersion of the glass chosen and with larger distance for the near object point.

OCIS codes: (220.2740) Geometric optical design; (220.1010) Aberrations (global), (080.0080) Geometric optics; (220.0220) Optical design and fabrication.

References and links

1. M. Born and E. Wolf, *Principles of Optics, 7th ed.* (Cambridge University, 1999).
2. H. Gross, *Handbook of Optical Systems, Volume 1, Fundamentals of Technical Optics* (Wiley-VCH, 2005).
3. M. Laikin, *Lens Design* (CRC Press, 2006).
4. E. R. Dowski and W. T. Cathey, "Extended depth of field through wavefront coding," Appl. Opt. **34**, 1859–1866 (1995).
5. W. Chi, K. Chu, and N. George, "Polarization coded aperture," Opt. Express **14**, 6634–6642 (2006)
6. H. Nagahara, S. Kuthirummal, C. Zhou, and S. K. Nayar, "Flexible depth of field photography," in *"European Conference on Computer Vision,"* (Springer, 2008), pp. 60–73.
7. R. Yokoya and S. K. Nayar, "Extended depth of field catadioptric imaging using focal sweep," in *Proceedings of the IEEE International Conference on Computer Vision* (2015), pp. 3505–3513.
8. S. Elmalem, N. Konforti, and E. Marom, "Polychromatic imaging with extended depth of field using phase masks exhibiting constant phase over broad wavelength band," Appl. Opt. **52**, 8634–8643 (2013).
9. B. Milgrom, N. Konforti, M. A. Golub, and E. Marom, "Novel approach for extending the depth of field of Barcode decoders by using RGB channels of information," Opt. Express **18**, 17027–17039 (2010).
10. H. Haim, A. Bronstein, and E. Marom, "Computational multi-focus imaging combining sparse model with color dependent phase mask," Opt. Express **23**, 24547-24556 (2015)
11. E. Ben-Eliezer, E. Marom, N. Konforti, and Z. Zalevsky, "Experimental realization of an imaging system with an extended depth of field," Appl. Opt. **44**, 2792–2798 (2005).
12. N. George and W. Chi, "Extended depth of field using a logarithmic asphere," J. Opt. Soc. Am. A **5**, S157 (2003).
13. H.-S. Chen and Y.-H. Lin, "An endoscopic system adopting a liquid crystal lens with an electrically tunable depth-of-field," Opt. Express **21**, 18079–18088 (2013).
14. S. Liu and H. Hua, "Extended depth-of-field microscopic imaging with a variable focus microscope objective," Opt. Express **19**, 353–362 (2011).
15. C. Perwass, L. Wietzke, "Single lens 3D-camera with extended depth-of-field," Proc. SPIE **8291**, 829108 (2012)
16. P. Mouroulis, "Depth of field extension with spherical optics," Opt. Express **16**, 12995–13004 (2008).
17. F. Guichard, H. Nguyen, R. Tessieres, M. Pyanet, I. Tarchouna, and F. Cao, "Extended depth-of-field using sharpness transport across color channels," Proc. SPIE **7250**, 72500N (2009).
18. C. Olsovsky, R. Shelton, O. Carrasco-Zevallos, B. E. Applegate, and K. C. Maitland, "Chromatic confocal microscopy for multi-depth imaging of epithelial tissue," Biomed. Opt. Express **4**, 732–740 (2013).
19. D. A. Atchison and G. Smith, *Optics of the Human Eye* (Butterworth-Heinemann Oxford, 2000).
20. W. T. Welford, *Aberrations of Optical Systems* (CRC Press, 1986).
21. C. J. Sheil and A. V. Goncharov, "Crystalline lens paradoxes revisited: significance of age-related restructuring of the GRIN," Biomed. Opt. Express **8**, 4172–4180 (2017)
22. R. Navarro, "Adaptive model of the aging emmetropic eye and its changes with accommodation," J. Vis. **14**, 21 (2014)

23. N. Fitzgerald, C. Dainty and A. V. Goncharov, "Extending the depth of field in a fixed focus lens using axial colour," Proc. SPIE **10590**, 1059034 (2017)

1. Introduction

A large depth of field is sought after for many applications in consumer imaging, such as increasing the range of focus for positioning the eye in iris imaging. With the increasing number of cameras in current consumer devices, implementing a dedicated camera for iris imaging must be introduced at a low cost and low power consumption. Common solutions include computational algorithms or mechanical refocussing which can be demanding on the device and increase the price of the camera module. In this paper, we introduce a cost-effective solution to refocussing of a front-facing camera in a mobile phone with longitudinal chromatic aberration. This method is aimed specifically at iris recognition for biometric authentication and it shows good promise for mass production.

Optical systems designed for imaging at fixed focus often have a relatively large depth of focus (in image space), e.g. if the detector is shifted axially from the paraxial focus by a minimum amount Δz, the image still remains sharp. Typically such systems have large f-number = f/D, that is, lenses with long f and small D, however modern optical systems require compact and light efficient designs as found in mobile phone camera lenses with f-number ranging from 2.8 to 1.7. To understand the limitation of these fast systems we shall start with the well-known formula for depth of focus, which corresponds to 80% reduction in the central intensity of the PSF or quarter wavelength wavefront error at the edge of the pupil as a result of defocus [1]:

$$\Delta z = \pm 2\lambda (F\#)^2, \tag{1}$$

where f-number $F\#$ is f/D, f is the focal length of the lens and D is the diameter of the entrance pupil.

The depth of field is an important concept in imaging systems, especially when is not available. The depth of field (ΔZ) defines the range of distances in object space for which the object remains sharp for a fixed sensor position:

$$\Delta Z \approx \Delta z / \bar{m}, \tag{2}$$

where the axial magnification from image space to object space is denoted by $\bar{m}$, typically in phone cameras $\bar{m} \ll 1$. For an imaging lens in air with a small depth of focus, Δz, the axial magnification is found as $\bar{m} = m^2$ [2], where m is lateral magnification defined as:

$$m = l_{image} / l_{object} \approx f/l, \tag{3}$$

f is the focal length and l is the object distance. Note that for $l \gg f$, we assume that image distance is $l_{image} \approx f$. From Eqs. (1) - (3) one can obtain the expression for depth of field:

$$\Delta Z = 2\lambda (f^2/D^2)(l^2/f^2) = 2\lambda (l^2/D^2) \tag{4}$$

The relation between pupil diameter and depth of field is clear, for a given object distance l, reducing pupil diameter results in extended depth of field (EDOF). However, in a more general case when the object is at a finite distance the symmetry in Eq. (1) is not preserved in Eq. (2), and one has to account for asymmetry in object space. Figure 1 shows the nominal image plane at point O' and symmetric displacement $\pm \Delta z$ on either side. The image point O' is conjugate to the object point O. As one can see depth of field is asymmetric such that the near distance, ΔZ°, is smaller than the far distance, ΔZ^*. Using the notation for the average depth of field, $\bar{Z} = 2\lambda l^2/D^2$ one can calculate ΔZ° and ΔZ^* more accurately (for $l \gg f$) with the following formulae:

$$\Delta Z^{\circ} = \bar{Z}(l - f)/(l + \bar{Z}) \tag{5}$$

$$\Delta Z^{*} = \bar{Z}(l - f)/(l - \bar{Z}) \tag{6}$$

Equation (4) gives the average value of the two, $\Delta Z = (\Delta Z^{\circ} + \Delta Z^{*})/2 = \bar{Z}$, which holds for $\bar{Z} \le l$, that is l is much smaller than the hyperfocal distance [3].
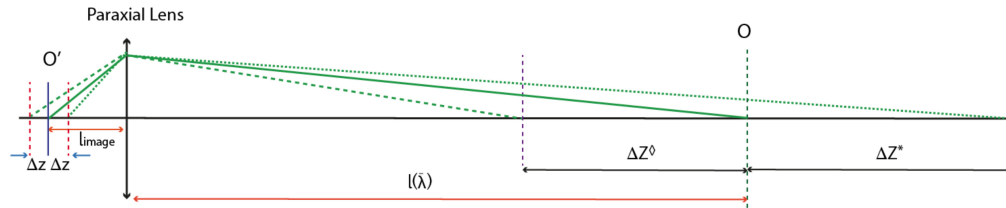

Fig. 1. Effective doubled depth of field for object position $l(\bar{\lambda})$.

Previous methods for extending depth of field in imaging systems include computational algorithms such as coded apertures which in practice require adding optical elements to the system for inducing aberrations that "hide" the change in the point spread function (PSF) due to variations in defocus. Computational methods employing phase masks for wavefront coding to alter the PSF and OTF so that both become invariant of object position [4] and [5]. Such imaging systems are capable of near diffraction-limited performance within the increased depth of field. Within a certain range of object distances the optical system produces an invariant PSF, which is known and thus allows one to deconvolve the blurry image to restore its sharpness without need to estimate the object distance [6] and [7]. A polychromatic phase mask for extending depth of field consists of annular rings designed to introduce a π-phase shift for all wavelengths and are called polychromatic composite masks (PCM) [8]. The PCM radii are optimised for a minimum cut-off frequency over the depth of field for three wavelengths in the visible region. An improvement in MTF performance can be seen at 450 nm and 650 nm at the expense of the performance at 550 nm. Two PCM elements of inverse profiles and different dispersion placed together in the pupil can achieve almost constant phase shift for the entire illumination bandwidth. An RGB phase mask can introduce three different phase shifts, one for each R, G and B, such that all colour channels are in focus for different regions in object space generating an extended depth of field [9]. Combining this approach with a post-processing, Haim et. al. deblurs the image produced by this RGB phase mask using a blur modelled as a piecewise-constant kernel which is defined by a defocus parameter of an object in the scene [10]. That is, the scene is divided into sections where each section is examined and restored independent of the other sections in the image. Multiple Fresnel lenses can mimic the effect of a phase mask, where each Fresnel lens in conjunction with the primary lens produces a sharp image at discrete locations along the optical axis [11]. The acquired image can produce a sharper image with a larger depth of field when compared with a clear-aperture lens of the same pupil size without the use of image post-processing. However, the authors acknowledge the reduction in resolution with the increase in the number of Fresnel lenses used.

Logarithmic aspheres together with post-processing employ a non-paraxial form of diffraction theory to create a desired PSF, that can be used to compute and fabricate a blurring phase filter or aspheric lens, which is then combined with a commercial lens [12]. Changing the geometrical

focus in real time using a liquid lens has been proven experimentally. Chen and Lin introduce a concept of an electrically tuneable liquid lens capable of producing three different lens powers and increasing the spatial depth perception to twice that of a conventional endoscope without the image post processing [13]. Liu and Hua require restoring algorithms for the variable focal objective for deconvolving the captured image to produce an EDOF effect [14]. Placing a micro lens array before the image plane can transform a single lens into a multi-focus plenoptic camera yielding an extended depth of field [15]. The plenoptic camera has three different types of micro lens sub arrays each having different focal lengths. The focal lengths are chosen so that each micro lens depth of field overlap and thus optimise the effective resolution over the extended depth of field. Reconstruction algorithms are then used to retrieve the EDOF image.

Utilising optical aberrations can aid the depth of field enhancement such as introducing spherical aberration by means of spherical optics [16]. In this paper the lens is achromatic over the visible range and rotationally symmetric blur induced in the image stays invariant across the field. As the position of the object is unknown, but lies within the EDOF region, the image deblurring is performed by applying a mean monochromatic PSF. Transverse chromatic aberration in the lens must be corrected for imaging in polychromatic light. Applications for extended depth of field using chromatic aberration has been implemented in confocal microscopy [18]. This application takes advantage of the longitudinal chromatic aberration from stock aspheric lenses.
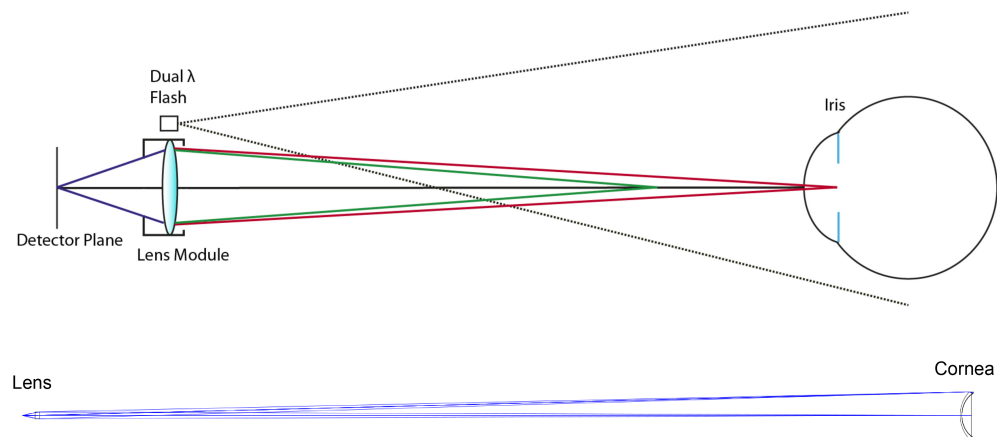

Fig. 2. EDOF concept: the dual-wavelength flash illuminates the iris which then reflects the NIR light. The lens is designed with a specific amount of axial chromatic aberration such that the iris image remains in focus in one of the two colours shown in the top schematic which is not to scale. Zemax raytrace to scale from the detector into object space showing the cornea and the iris.

Various object distances can be resolved from induced axial colour with post-processing and sharpness metrics across colour channels [17]. Each colour corresponds to a particular object distance, and thus a depth map can be produced such that each colour is reconstructed based on the filtering parameters assigned to the respective colour. In contrast to this approach, we introduce a method that also relies on intrinsic longitudinal chromatic aberration to extend the depth of field by means of a dual-wavelength illumination, see Fig. 2. The key difference is that the sharp image is obtained in real time without computational intensive algorithms. The main goal is to design a low-cost lens in a front-facing camera in mobile phones for iris recognition. The cost-effective solution is obtained by avoiding refocussing systems with voice coils that can increase the cost of the camera module in a mobile phone by 10 %.

2. The concept of dual-wavelength imaging of the iris

The choice of wavelength for iris illumination is determined by the physical properties of the iris. In the near infrared (NIR) the iris shows more detail, which is essential for iris recognition and authentication of the user [19]. Another advantage of illuminating in the NIR is the fact that in this spectral region there is a reduction in solar radiation, which helps to reduce the unwanted NIR background in daylight imaging (λ = 880 nm to 920 nm).

We shall present the concept of EDOF using dual-wavelength illumination by considering a plano-convex singlet. Iris illumination is formed by two commercial NIR LEDs, λ_1 and λ_2, of known bandwidth $\Delta\lambda$, where $\lambda_1 < \lambda_2$ and $\Delta\lambda \ll \lambda_2 - \lambda_1$. In a conventional singlet lens, dual-wavelength illumination introduces longitudinal chromatic aberration (LCA). However, one can exploit that feature (taking in to account the dispersive nature of the glass) when optimising LCA of the lens. Without changing the position of the image plane one could form either sharp image at λ_1 from a near distance and image at λ_2 from a far distance with both images being sharp at $(\lambda_1 + \lambda_2)/2$ object distance. A design method for a plano-convex singlet lens is presented below.
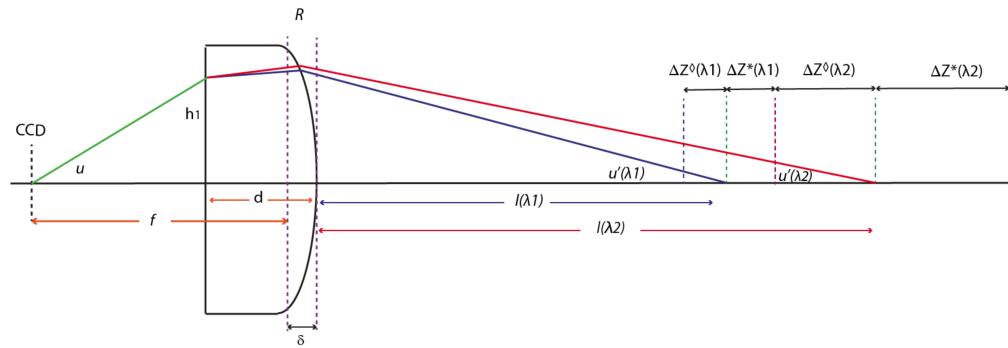

Fig. 3. Extending depth of field in a plano-convex singlet by means of longitudinal chromatic aberration.

Analytical derivation of lens parameters

To describe our analytical method we start with paraxial raytracing using Welford's notation [20]:

$$n'_j u'_j - n_j u_j = -h_j \phi_j \tag{7}$$

$$h_{j+1} = h_j + u'_j d'_j, \tag{8}$$

where u is marginal ray angle, h is ray height at the surface and ϕ is the optical power of the surface, described as $\phi_j = (n'_j - n_j)/R_j$ with R_j being the radius of curvature. The refractive index of the medium before and after the surface is denoted by n_j and n'_j, respectively. Figure 3 shows the raytrace of a marginal ray through a plano-convex lens at wavelength λ_1 and λ_2. Note that raytracing is reversed, that is the ray starts at the detector and propagates through the lens into object space. The principal planes of the singlet are drawn by dashed purple lines, where the front principal plane coincides with the vertex of the front surface. The second principal plane can be found by determining the separation of the planes, δ, known as the interstitium [20].

Following the sign convention in optics, the radius of curvature for the posterior refracting surface of the singlet in air is negative ($R_j < 0$), and the optical power of the surface is:

$$\phi_j = (1 - n_j)/R_j \tag{9}$$

In the case of a plano-convex singlet, Eq. (9) determines the overall optical power of the lens. Reverse raytracing allows us to derive an expression for the final angle $u'(\lambda_1)$ and $u'(\lambda_2)$ at wavelengths λ_1 and λ_2, which correspond to different object positions due to LCA, see Fig. 3. The intrinsic amount of chromatic aberration in a singlet is denoted by the difference in chromatic object positions, $\Delta l = l(\lambda_2) - l(\lambda_1)$, where $l(\lambda_1)$ is given by design specification, which in turn determines the radius of curvature R in the singlet for a chosen refractive index, $n(\lambda_1)$. The far object point $l(\lambda_2)$ is determined by raytracing, once the material for the lens is selected and dispersion in the NIR is known (see our discussion on glass vs plastics).

Using paraxial raytracing Eqs. (7), (8) one can derive the ray path through the singular plano-convex lens for λ_1 and λ_2 as:

$$u'(\lambda_1) = 1/f(\lambda_1) + (n(\lambda_1) - 1)/R = -1/l(\lambda_1) \tag{10}$$

and

$$u'(\lambda_2) = 1/f(\lambda_2) + (n(\lambda_2) - 1)/R = -1/l(\lambda_2) \tag{11}$$

To find the focal length f present in Eqs. (10) and (11), we note first that the separation of the principal planes δ is found as:

$$\delta(\lambda) = d - d/n(\lambda) \tag{12}$$

where d is the central thickness of the lens. Note that Eq. (12) is an approximation since the quadratic term with respect to d has been omitted. Using Eq. (12) and selecting the distance from the detector to the flat surface of the lens, which is the back focal distance (BFD) in imaging mode, the focal length of the lens is found as:

$$f(\lambda) = BFD + d/n(\lambda), \tag{13}$$

which is shown in Fig. 3. For a given $l(\lambda_1)$, the radius of curvature is found from Eq. (10):

$$R = f(\lambda_1)l(\lambda_1)(1 - n(\lambda_1))/(f(\lambda_1) + l(\lambda_1)) \tag{14}$$

For selected lens material (dispersion) and λ_2, one can calculate $n(\lambda_2)$ and find $l(\lambda_2)$ from Eqs. (14) and (11):

$$l(\lambda_2) = R/(1 - n(\lambda_2) - R/f(\lambda_1)) \tag{15}$$

The method presented above provides three lens parameters, namely, f, R and $l(\lambda_2)$ when λ_1, λ_2, lens material, $n(\lambda_1)$, $n(\lambda_2)$ as well as BFD and d are known from lens specification. The depth of field associated with both object positions must overlap to ensure sufficient sharpness over the extended region $\Delta l + \Delta Z^\circ(\lambda_2) + \Delta Z^*(\lambda_1)$ in object space, see Fig. 3. To avoid excessive defocus in the mid region one requires to fulfill the condition for having no gap between $\Delta Z^*(\lambda_1)$ and $\Delta Z^\circ(\lambda_2)$, that is $\Delta Z^\circ(\lambda_2) + \Delta Z^*(\lambda_1) \geq \Delta l$. Using the approximation for depth of field $\Delta Z^\circ = \Delta Z^* = \Delta Z$, where ΔZ is found from Eq. (4), assuming $\lambda = \lambda_1$, we can find the largest pupil diameter that satisfies this condition: $2\lambda_1(l^2(\lambda_1)/D^2 + l^2(\lambda_2)/D^2) \geq \Delta l$, which is equivalent to: $D^2 \leq 2\lambda_1[l^2(\lambda_1) + l^2(\lambda_2)]/\Delta l$. The condition for f-number becomes :

$$F\#^2 \geq f^2\Delta l/2\lambda_1[l^2(\lambda_1) + l^2(\lambda_2)] \tag{16}$$

If the f-number from Eq. (16) is too large (the lens is too slow), one could reduce λ_2 and hence decrease Δl at the price of reducing the effect of EDOF in the lens design. There is a trade-off between increasing Δl and attaining competitively low f-number.

3. Optical system examples

The validity of this method can be demonstrated using two examples: a plano-convex lens made of highly dispersing flint, N-SF5, and a moulded plastic, E48R. For our lens imaging the iris at $\lambda_1 = 780 \pm 15$ nm and $\lambda_2 = 870 \pm 20$ nm, a highly dispersive glass is chosen to maximise the longitudinal chromatic aberration in object space, thus leading to a larger depth of field. N-SF5 glass is a dense flint and has an Abbe number of 32.2. The thickness of the singlet is set to $d = 1.5$ mm. The BFL is 4 mm and the near object distance is $l(\lambda_1) = 300$ mm.

Using Eqs. (13) - (15) we find the parameters for the lens as $f = 4.90$ mm, $R = -3.182$ mm, $l(\lambda_2) = 432.37$ mm and $\Delta l = l(\lambda_2) - l(\lambda_1) = 132.37$ mm. The condition for f-number from Eq. (16) leads to $F\# \geq 2.72$, taking the smallest value $F\# = 2.72$, the corresponding diameter of the lens is $D = 1.8$ mm. The approximate formula predicts the depth of field as $\Delta l + 2(\lambda_1 l(\lambda_1)^2 + \lambda_2 l(\lambda_2)^2)/D^2 = 275$ mm. Note that at the near object distance $l(\lambda_1)$ the $F\#$ and working $F\#$ differ by approximately 1.5% and this discrepancy is to some extent compensated by the approximation made in Eq. (12). The exact value for the focal length verified in Zemax is $f = 4.825$ mm with corresponding f-number for an object at infinity is $F\# = 2.68$ and working f-number = 2.72.
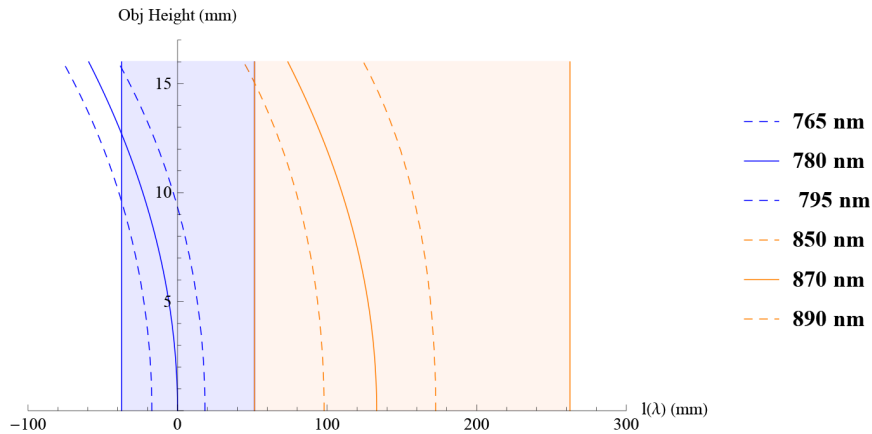

Fig. 4. Plot in object space showing the depth of field for an N-SF5 singlet fulfilling the criterion. Solid lines indicate the optimum position of the eye with respect to the camera.

Using Eqs. (5) and (6) the exact depth of field is $\Delta l + \Delta Z^\diamond(\lambda_1) + \Delta Z^*(\lambda_2) = 302$ mm, as seen in Fig. 4, where the near object point is taken as the origin for the horizontal axis. Depth of field at the far object point is 2.4 times longer than that of the near object point. Thus it is always more challenging to extend depth of field at near object distances.

For a single wave illumination at $\bar{\lambda} = (\lambda_1 + \lambda_2)/2$, which corresponds to the object distance $l(\bar{\lambda}) = 359.8$ mm, depth of field is $\Delta Z^\diamond(\bar{\lambda}) + \Delta Z^*(\bar{\lambda}) = 144.6$ mm. For this average wavelength $(\bar{\lambda})$, lens design with the dual wavelength illumination offers depth of field 2.09 times longer than that of single wavelength (λ_1) illumination design. Most importantly this extended depth of field allows the user to exploit object distances in a closer proximity to the lens.

The singlet is assigned two aspheric surfaces, described by the following equation:

$$z = y^2/2R + Ay^4 + By^6 \qquad (17)$$

The front surface of the lens has $A = 1.6736x10^{-3}$, $B = 2.877x10^{-4}$ and conic constant $k = -1$. The posterior surface has a conic constant $k = -1$, $A = 2.7392x10^{-4}$ and $B = 6.9758x10^{-4}$. Two aspherical surfaces allow to correct for spherical aberration and coma. The full field of view is
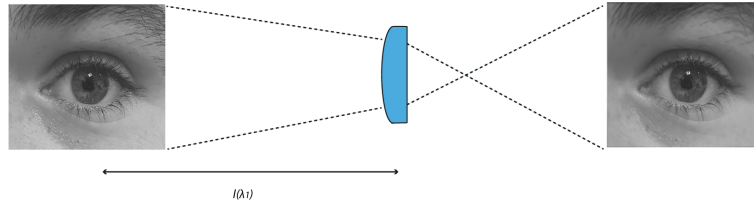
Fig. 5. Iris imaging with an aspheric, plano-convex singlet lens. The features of the iris required for identification remain sharp, while the effect of astigmatism is noticeable outside the central field. For comparative purposes the object and image are the same size and orientation

limited by astigmatism to approximately 6 deg (attaining diffraction-limited image quality). At the near object distance, $l(\lambda_1)$ the maximum object size is 32 mm (for 6 deg flat field), which is sufficient to image the full iris of a single eye.
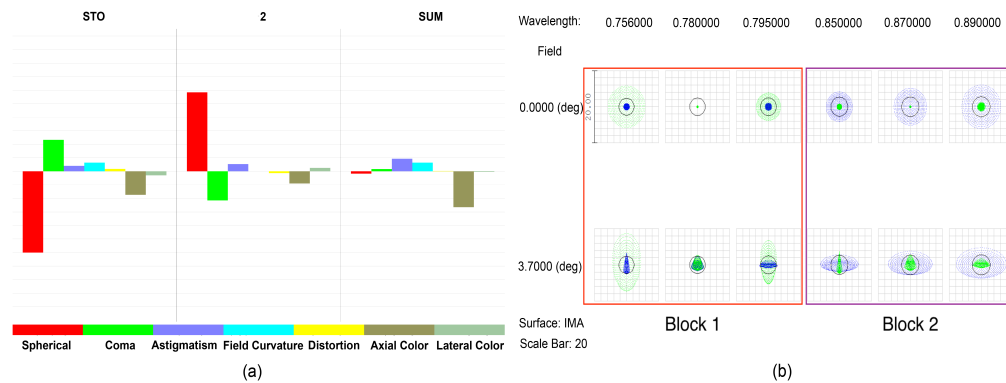

Fig. 6. (a) Seidel aberrations for the high dispersion N-SF5 singlet in image space. Maximum aberration scale is 0.00500 mm. (b) The Block 1 and 2 of spot diagrams for the dual flash illumination on the image plane. The Airy disk is shown in black with a radius of 2.376 μm.

Figure 6 shows the aberration correction on the detector (lens is in the imaging mode). The image quality is limited by astigmatism, but this does not compromise the centering of the eye on the detector as can be seen from Fig. 5, where we used Zemax program to simulate the impact of the lens aberrations on the image of the eye. Axial colour resulting from the finite bandwidths (30 and 40 nm) of the illumination sources is well within the depth of focus and does not reduce image quality of the lens, see Fig. 4. For aberration analysis in Fig. 6 we assumed that the object is not a plane but a paraboloid of revolution with 1.63 mm radius of curvature at the vertex, λ = 780 nm. This object surface indicates the optimum off-axis eye placement with respect to the lens when one needs to take into account the curvature of the object field as indicated by the solid lines in Fig 4. The iris is modelled as a flat surface. This allows one to widen the field of view to approximately 8° and also account for protruding facial features such as the eyebrow and nose.

The spot diagrams for the two object distance $l(\lambda_1)$ and $l(\lambda_2)$ shown in Fig. 6(b) are plotted for on axis and approximately 4 deg off-axis field at six wavelengths, λ_1 = 780 ± 15 nm and λ_2 = 870 ± 20 nm. Block 1 shows six spot diagrams for near distance $l = l(\lambda_1)$ being in focus (λ_1 shown in blue), with the upper row for on axis and lower row for 3.7 deg off-axis field point. Block 2 corresponds to far object distance $l = l(\lambda_2)$ being in focus (λ_2 shown in green). Spherical aberration and coma are well balanced, whereas astigmatism and axial colour are present, as can be seen in bar diagram for Seidel aberrations in Fig. 6(a).

Table 1. N-SF5 glass and E48R optical plastic aspheric singlets with parabolic object surface.

	$n(\lambda_1)$	$n(\lambda_2)$	f	R	$l(\lambda_2)$	Δl	D	F#	$2\,\omega$
N-SF5	1.6595	1.6560	4.90	-3.182	432.36	132.36	1.9	2.7	7.5°
E48R	1.52505	1.52348	4.98	-2.573	361.74	61.74	2.36	2.1	6°

The illumination scheme is such that the image is obtained in a sequential manner. The sharper image can be selected based on sharpness criterion or the interpupilary distance if it can be found from the image. In practice, the method with the least power consumption will be chosen. For the mid position where both images are equally defocussed, we take the image with the longer distance flash which grantees more flux and smaller signal to noise ratio.

An optical polymer can also be used as an example to explore the feasibility of extending depth of field. E48R from the *Zeon* catalogue has an Abbe number of 56.04, thus having a similar dispersive nature to a crown glass such as N-BK7. Table 1 lists lens parameters for both lens designs for comparison. Since the plastic material is less dispersive than N-SF5 glass, the plastic lens has a smaller Δl = 61.74 mm for the same illumination sources. As a result one can use an f-number as fast as 2.1.
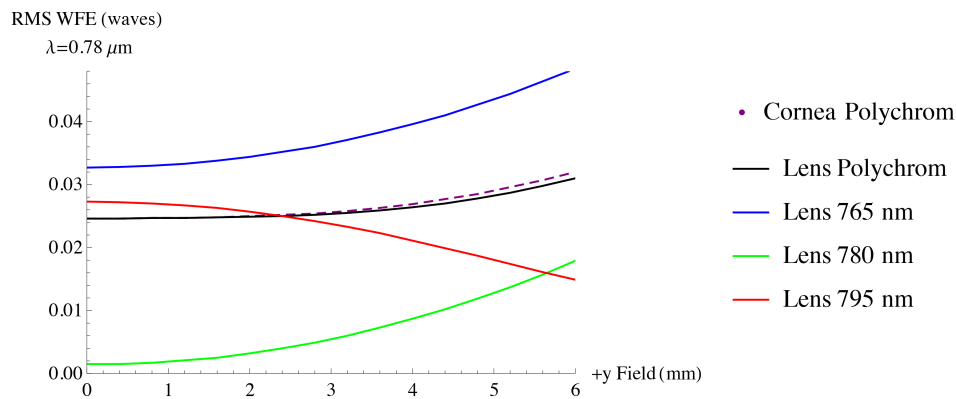

Fig. 7. Rms wavefront error vs field for the singlet illuminated by $\lambda_1 \pm \Delta\lambda$. The effect of introducing the cornea on the rms wavefront error is seen by the dashed purple line.

The cornea was modelled in Zemax with data from previously published papers [21, 22]. Figure 7 shows the rms wavefront error in waves for $\lambda_1 \pm \Delta\lambda$, see Fig. 2. The diffraction limit of the system when imaging through the cornea is 0.072 waves (0.056 μm at λ_1 = 780 nm). A minimum of 2 cy/mm is required to image the fine details of the iris which corresponds to 150 cy/mm on the detector. Figure 8 is the MTF of the lens and cornea where the modulus of the OTF at 150 cy/mm is 0.56. In our model, the presence of the cornea does not compromise image quality. A -9% distortion was induced by imaging through the cornea which can be easily corrected computationally as distortion does not blur the image. We also assume here that the detector has a pixel size of 1.19 μm to satisfy the Nyquist sampling criterion for the Airy disk radius of 2.38 μm.

4. The impact of lens shape factor and near object position

Optimising for a parabolic object surface allows one to have additional depth of field by decentering the eye and bringing it closer to the lens. That is by increasing the height in object
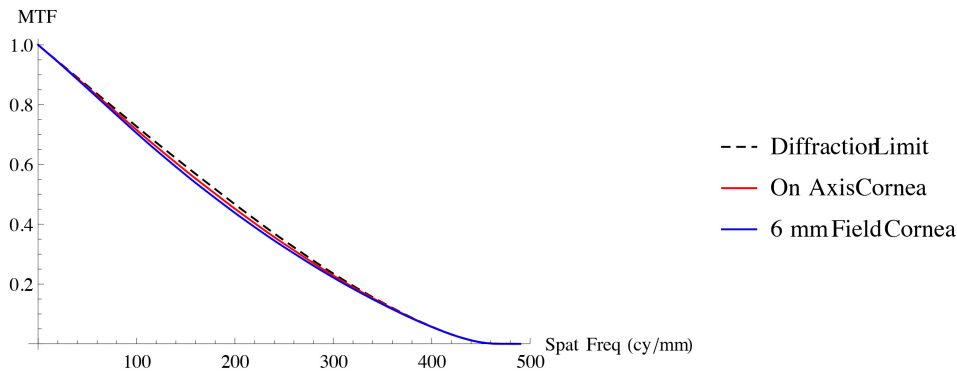
Fig. 8. MTF for singlet lens and cornea.

space and following the curvature of the parabolic surface, see Fig. 4, one gains extra depth of field at the near object point. However, this parabolic surface lies between tangential and sagittal foci (for lens working in reverse mode). Therefore, with increasing object height the possibility of imaging the iris as a whole becomes more challenging due to the astigmatism. The image quality of the iris imaged at 15 mm off-axis when the eye is positioned on the parabolic surface with a radius of 1.63 mm at 240 mm, shown in Fig. 9, gaining additional 60 mm in depth of field at the near object point.

The plano-convex singlet presented in this paper is chosen for the requirement of having F# $\leq$ 2.7. We have considered the use of other singlet lenses with different shape factor and studied its impact on our application, seen in Fig 10. A singlet with a back surface being concentric to the lens focus can offer a small reduction in Δl. For this lens design, the effect of each wavelength on object distance l can be calculated using the equation: $n(\lambda)/(BFD+d)+(1-n(\lambda))/R = -1/l(\lambda)$, where the front radius R is solved as a function of λ_1 and then one could find $l(\lambda_2)$ as a function of λ_2 and R. Reversing the orientation of the plano-convex lens such that the planar surface is facing the object has the capability to increase Δl and field of view shown in table 2. The radius of curvature and
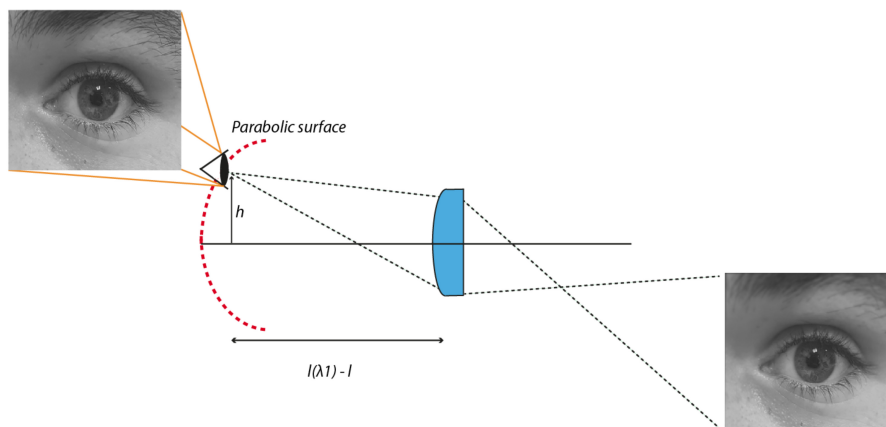

Fig. 9. Iris imaging with a aspheric, plano-convex singlet lens centred at object height 15 mm positioned on the parabololic object surface at a distance 240 mm from the lens where l is the sag of the parabola at h=15 mm.

far object point $l(\lambda_2)$ can be calculated from $u'(\lambda) = 1/f(\lambda) + (n(\lambda) - 1)/R = -1/(l(\lambda) - d/n(\lambda))$ where R and $l(\lambda_2)$ are found as a function of λ_1 and λ_2 respectively.

Table 2. Shape factor: Lens data for N-SF5 singlet where CP for the object surface as a parabola, FP is a flat object plane and SF is shape factor

Singlet	Concentric	Plano-Convex	Rev Plano-Convex	Meniscus
Δl	126.1 mm	132.37 mm	202.79 mm	230 mm
2ω CP	7.4 °	7.4°	12.8°	13°
2ω FP	6 °	6.5°	9.8°	10.3°
F #	2.6	2.7	3	3.1
SF	3.35	-1	1	-1.30

Freeing both radii in a singlet lens allows one to find an optimum lens shape for best aberration correction. In this case, the front object point is anchored at $l(\lambda_1)$=300 mm and the lens is optimised for parabolic object surface. The singlet lens geometry converges to a negative meniscus lens with an increased diffraction limited field to 13° and 10° for plane object. The separation of object points, Δl, increases to approximately twice Δl of the initial plano-convex lens example. This extension in Δl occurs at the expense of increased f-number, as larger Δl requires a slower lens see. Table 2 includes a list of design parameters for different shape factors of a singlet made from N-SF5 having different shape factors, $SF = (R_2 + R_1)/(R_2 - R_1)$. Each singlet lens requires an optimised parabolic object surface with a specific radius given in Ref. [23].

Special constraints must be introduced when applying this methodology to the visible spectrum. LCA in the visible region must be controlled such that Δl does not exceed a certain value to avoid a slow lens associated with a larger Δl. The separation of LED central wavelength of the two sources can be reduced to 50 nm in the yellow region of the spectrum where slope of refractive index versus wavelength is not as steep compared to the blue region, thus one could achieve a reasonable f-number. Additionally, materials of high Abbe number can be chosen inducing low
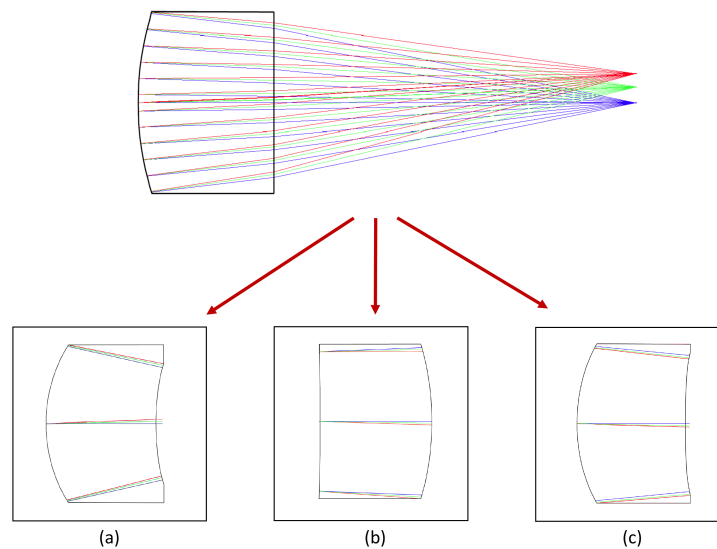

Fig. 10. Singlet lenses in imaging mode: (a) concentric surface singlet, (b) reverse plano-convex singlet and (c) meniscus singlet.
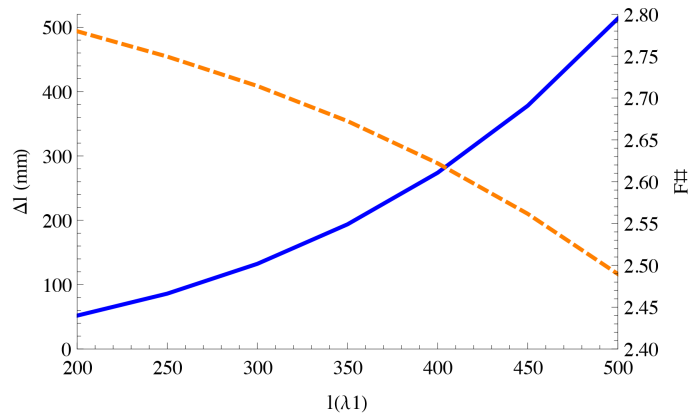
Fig. 11. Changes to f-number and Δl as the distance of the near object point is varied. The solid blue line corresponds to Δl vs $l(\lambda_1)$ and the dashed orange line represents $F\#$ vs $l(\lambda_1)$.

dispersion that brings Δl to similar values as we presented for the NIR region. Alternatively, one could consider introducing two elements with a partial compensation of axial chromatic aberration to gain better control of chromatic aberration in the visible.

It is interesting to note that one could also vary the near object distance to control Δl, however as one can see from Fig. 11 bringing near point closer to the lens reduces Δl and depth of field and at the same time increases f-number which again shows the challenge of extending the depth of field at regions closest to the lens.

5. Conclusion

We have presented an analytical method for extending the depth of field in fixed focus lenses using dual flash illumination. With this method singlets with various shape factors have been explored and analysis of their optical performance is presented. Introducing curvature of the object surface allows for a larger field of view and offers additional distance to the EDOF region by decentering the eye. The field attainable in a singlet is sufficient for imaging a singular eye.

Funding